

Influence of local structural distortion on the magnetism of Na₂IrO₃ compoundsM. A. Tovar-Olvera  and Pedro Ruiz-Díaz ^{*}*Instituto de Física, Universidad Autónoma de San Luis Potosí, Álvaro Obregón 64, Centro, 78300 San Luis Potosí, S.L.P. México*Matthieu Saubanère *ICGM, Université de Montpellier, CNRS, ENSCM, Montpellier 34000, France
and Réseau sur le Stockage Electrochimique de l'Énergie (RS2E), CNRS, Amiens 80000, France*

(Received 24 May 2021; revised 13 September 2021; accepted 1 March 2022; published 10 March 2022)

First-principles calculations are conducted to investigate the magnetic properties of the Na₂IrO₃ compounds. We reveal that the Na₂IrO₃'s local structural distortions are essential for an accurate description of the magnetism of such systems. They provide a feasible explanation for the experimentally observed antiferromagnetic zigzag magnetic ground state. We demonstrate that the underlying competition between the spin-orbit coupling and the crystal-field splitting rules the crystal structure and profoundly influences the strength of the magnetic exchange interactions. We unambiguously identify that the D_{4h} -type distortions, due to the Jahn-Teller effect, are disclosed in an elongation along the IrO₆ polyhedra's apical axis in the ac plane. On the other hand, the Ir atoms off-centering in the basal plane (perpendicular to the local D_{4h} elongation axis) arises owing to an inhomogeneous cationic charge distribution of Ir⁴⁺/Na⁺ in the transition-metal layer resulting in both effects being decisive in controlling the magnetism of Na₂IrO₃ together with the spin-orbit interactions.

DOI: [10.1103/PhysRevB.105.094413](https://doi.org/10.1103/PhysRevB.105.094413)**I. INTRODUCTION**

The layered-honeycomb hexagonal lattices compounds [A_x(TM)O₃, A = alkali-metal] provide an exciting playground for investigating complex magnetic arrangements [1–19]. In particular, the Ir-based layered oxides (iridates) are of great interest due to their large spin-orbit coupling [13,20–29]. Hence, iridates may exhibit intricate magnetic textures as several competing interactions can be identified: geometrical frustrations due to the Ir honeycomb's lattice, electron-electron correlations, strong spin-orbit coupling (SOC), and long-range van der Waals interactions yielding to manifold unconventional magnetic phases, such as structural phase transitions or spin-liquid states [7,11,30–32].

Moreover, in the A₂IrO₃ structure, the Ir⁴⁺(d⁵) ions have a half-filled d shell, which remains degenerated upon considering the crystal-field splitting (CF) due to their octahedral environment. As shown in Fig. 1, this remaining unphysical degeneracy can be further removed by either considering the spin-orbit interactions or lowering the local structural symmetry through Jahn-Teller (JT) distortions [33]. Indeed, the JT effect results in a broken degeneracy of the t_{2g}/e_g orbitals that follow a D_{4h} -type distortion. Consequently, the competition between the SOC interactions or JT-like distortions determines the character and shape of the magnetization density, which is expected to profoundly influence the spin-exchange interactions and thus the magnetic ordering at low temperatures [34]. It is commonly assumed that SO interaction dominates over the CF splitting on the iridates [24,35,36]. Therefore, the local structural distortions are often neglected from the magnetic behavior's description due to their inherent

complexity to be treated. Most of the models used to investigate the iridates' magnetic behavior are formulated without considering local distortions. In these models the t_{2g}/e_g orbitals are written in terms of the $J_{\text{eff}} = 1/2$, $3/2$ and $J_{\text{eff}} = 5/2$ relativistic orbitals [37]. These descriptions are referred to as pseudospin or effective spin (J_{eff}) models.

Among the iridates, Na₂IrO₃, a weak insulator having a 340 meV band gap [38] and strong spin-orbit coupling, is an appealing example of a shared-edge octahedral system for which all the interactions mentioned above come into play, as they might have the same order of magnitude [39]. Na₂IrO₃ has a low temperature-ordered magnetic ground state, as shown in combined studies with neutron and x-ray diffraction on a single crystal [35,36,40]. Experimental measurements estimate that the local magnetic moments on the Ir⁴⁺ ions order below 12–18 K into zigzaglike magnetic chains along the $g \sim a + c$ axis of the honeycomb structure displaying a relatively small magnetic moment of $\langle \mu \rangle = 0.22 \mu_B/\text{Ir atom}$ [35,36,39,40]. Different scenarios can be undertaken regarding the dominant interactions for a comprehensive description of the magnetic properties of these compounds. If the JT-induced distortions overcomes the SOC interactions, one would then expect a quenching of the orbital moment and a D_{4h} splitting resulting in a $J = S$ system, and the magnetization density would be oriented perpendicularly to the D_{4h} elongation axis. On the other hand, if the SOC is dominant, then no local structural distortions would be expected, and the magnetization density would follow pseudospinlike models. Interestingly, if the JT-induced distortions and the SOC splitting are on the same order of magnitude in energy, then we would deal with a pseudo-Jahn-Teller effect, in which an orbital-lattice coupling modulates the shape of the pseudospin wave function usually used to describe $J_{\text{eff}} = 1/2$ systems [11,41]. However, it has been suggested that in

^{*}Corresponding author: prudi@ifisica.uaslp.mx

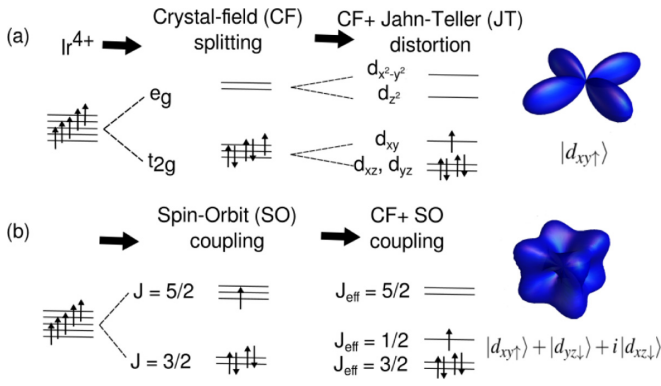


FIG. 1. Sketch of the dominant interactions and their effects (energy splitting) on the electronic structure of the Na₂IrO₃ compounds. (a) Crystal-field splitting and crystal-field + Jahn-Teller distortions on the electronic configuration of the Ir⁴⁺ ions together with the electronic charge-density profile. (b) Energy-splitting contributions for $J_{\text{eff}} = 1/2$ systems.

those models, the orbital nature of the bands near the Fermi level deviates from the spin-orbit coupling-induced $J_{\text{eff}} = 1/2$ states due to the hopping interaction and the *final* state can be better conceived as a mixture of the $J_{\text{eff}} = 1/2$ states and $J_{\text{eff}} = 3/2$ valence states of the Ir atoms [42]. Therefore, the JT-induced distortions and SOC competition has regained substantial interest as recent studies have highlighted its complexity, pinpointing the significance of the magnetoelastic coupling even in the strong SOC regime [11,43]. Liu *et al.* [11] argue that in the $J_{\text{eff}} = 1/2$ system for Sr₂IrO₄ these pseudo-JT effect terms induce tetragonal-to-orthorhombic structural transitions, which were crucial for understanding the observed magnetic properties, despite the pseudospin-lattice weak coupling terms. Moreover, Streltsov and Khomskii [43] reported that for a d^5 system, the SOC interactions might quench the JT effects above some critical value λ_c of the SOC strength. Below λ_c , the JT-induced structural distortions remain, bringing an anisotropic character of the magnetic interactions depending on the bond's directionality. Sometimes the interplay which exists between the JT distortions and the SOC in the magnetism for some honeycomb TM layered oxides is even more subtle than the competition between both effects. No general guideline can be drawn. In addition, some theoretical density functional theory-based studies have stressed the importance of having an accurate crystal structure, which is imperative as the spin-lattice coupling in highly frustrated systems may lead to more profound effects as, for instance, the spin orientation seems to be extremely sensitive to the crystal structure [44,45].

At this point, one must be aware that predicting the magnetic properties of spin-orbital-lattice entangled compounds is a rather complex task since one needs to deal with the spin interactions, electronic correlations, and JT-induced instabilities on the same footing. Attempting to provide convincing explanations for experimental measurements, such as the insulating band gap [46], magnetic ordering [40], and magnetic easy-axis orientation [47], numerous theoretical studies have been performed at different levels of approximation. Usually, complementary techniques are used, which are the focus on the realization of models based on the construction

of parametrized effective Hamiltonians either from first-principles [48] calculations or tight-binding models [34,49], although some more sophisticated methods such as the two-dimensional density matrix renormalization group and an infinite-size tensor-network method have been employed [50]. In summary, to explain the experimental antiferromagnetic zigzag magnetic configuration, the models can be grouped into (a) Heisenberg-Kitaev (HK) models which only consider first nearest-neighbor interactions (NN) [32,47], (b) HK models considering long-range interactions (usually second and third NN-interactions) [24,35,39], (c) modified HK models with only first NN interactions [51], and (d) quasimolecular orbital models [20,52–54].

In particular, within the HK model, it has been reported that the NN interaction, i.e., the Kitaev exchange, together with off-diagonal terms (such as the Dzyaloshinskii-Moriya interaction) and interactions beyond the NN range are all required for the low-temperature zigzag magnetic-state stabilization of Na₂IrO₃. Hou *et al.* [24] proposed a minimal J_1 - K_1 - Γ_1 - J_3 model for Na₂IrO₃, in which surprisingly a competition was found between non-neglectable third NN interactions ($J_1/J_3 \approx 2$) and the off-diagonal NN exchange terms. Also, Winter *et al.* [54], using nonperturbative exact diagonalization methods, identify significant long-range couplings (in particular, meaningful J_3 's) for Na₂IrO₃, α -RuCl₃, and α -Li₂IrO₃, which are essential to explain in a natural way the observed zigzag ordered phases of these compounds. Generally, in the J_{eff} models, structural distortions are not considered due to the involved complexity. The experimentally measured crystal structural distortions and quenched magnetic moment suggest that the competition between the J_{eff} and the quasimolecular nature of the p and d orbitals in Na₂IrO₃ should not be ignored, resulting in an orbital selectivity that could have a non-negligible impact to the magnetism on iridates even in the strong SOC regime. Besides, without considering local structural distortions and owing to the quasi-isotropic character of the magnetization density in the $J_{\text{eff}} = 1/2$ system, the occurrence of the canted zigzag magnetic order is surprising. The present work's aim is to investigate the impact of the local structural distortions on the magnetism of Na₂IrO₃. We identify and quantify the local structural distortions which strongly influence the magnetic interactions and rule the magnetic ordering. Remarkably, we show that SOC does not fully overcome JT distortion in these compounds so that the effect of the structural distortions remains essential even at the strong SOC regime to determine the magnetic interactions and, therefore, the magnetic order.

II. METHODOLOGY

First-principles calculations have been performed within the framework of the density functional theory (DFT) using a supercell approach as implemented in the Vienna *ab initio* simulation package (VASP) [55–58]. For the exchange-correlation energy functional, the Perdew-Burke-Ernzerhorf (PBE) generalized gradient approximation (GGA) [59,60] is employed. We used the projector augmented wave (PAW) method [61,62] together with an energy cutoff of $E = 800$ eV and k -mesh density of 0.21 K points/atom for sampling the Brillouin zone. For the nonrelativistic calculations, the

convergence energy criterion was set to 10^{-5} eV. Structural optimizations were performed by applying the conjugate gradient method until the forces in all atoms were less than 10^{-2} eV/Å. To compensate for the known overdelocalization of the electrons in DFT, we utilized the rotationally invariant approach to the DFT+ U method described by Dudarev [63]. A meticulous analysis regarding the influence of the effective on-site Coulomb repulsion term U_{eff} has been performed, see Table S1 and Fig. S1 of the Supplemental Material [64]. Here, unless specified, we employ $U_{\text{eff}} = 2$ eV which seems to be a suitable value to reproduce the magnetic properties of Na_2IrO_3 reported in the literature [44]. To take into account the long-range interactions, we included van der Waals corrections using the DFT-D3 method with Becke-Jonson damping [65,66]. To calculate the crystal orbital overlap population (COOP), we used the Lobster code implemented by the Dronskowski group [67–71]. When taking into account the SOC interactions, noncollinear self-consistent and non-self-consistent fixed-structure relativistic calculations were performed having a convergence energy criterion of 10^{-7} eV. Such energy criterion assures us to obtain well-converged reliable results.

A. Crystal structure and structural-distortion model

As shown in Figs. 2(a) and 2(b), Na_2IrO_3 's crystal structure is experimentally found in the $C2/m$ space group, and it is organized as a stacking of a pure Na layer and a NaIrO layer hereafter called transition metal (TMO) layer. The TMO layer displays a honeycomb arrangement of distorted edge-sharing IrO_6 octahedra. The structure possesses both orthorhombic and trigonal distortions, introducing a disproportion among the NN Ir-Ir and Ir-O distances and a 90° offset in the Ir-O-Ir angles. Thus, Na_2IrO_3 turns out to be an archetype of a system in which slight variations on its crystal structure can dramatically affect its local electronic structure [20], making it crucial to understand the structural-distortions effects on the underlying magnetism of these compounds at a fundamental level. From the experimental crystal structure [26,35,36], it is possible to identify two structural local distortions which have different origins and might have a strong influence on the magnetic interactions and, thereby, on the magnetic ordering. On the one hand, the D_{4h} -distortion type due to the JT effect is reflected in an elongation along the IrO_6 polyhedra's apical axis in the ac plane, as shown in Fig. 2(c). Interestingly, as a result of the anisotropic electrostatic potential arising from the compound's 2D-layered nature [see Fig. 2(c)], all local D_{4h} elongation axes are aligned, this axis is denoted later as the D_{4h} elongation axis. This alignment was experimentally observed [26,35,36] and also reproduced in our calculations as will be shown later on. On the other hand, we have the Ir atoms off-centering in the basal plane (perpendicular to the local D_{4h} elongation axis) observed as well in the experimental structure, owing to the inhomogeneous cationic charge distribution of $\text{Ir}^{4+}/\text{Na}^+$ in the TMO layer (see Fig. S2 in the Supplemental Material [64]). Indeed, using a point-charge model, the electrostatic energy decreases as a function of the Ir atoms off-centering. This inhomogeneous cationic charge distribution results in two different Ir-O bond distances on

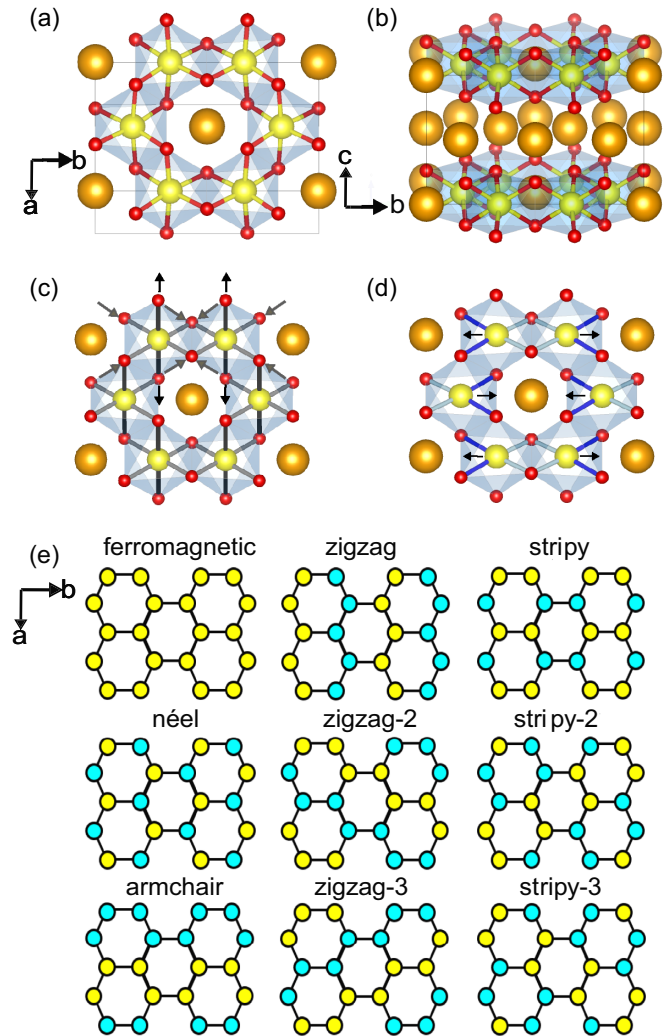


FIG. 2. (a) and (b) Crystal structure of $C2/m$ Na_2IrO_3 honeycomb structure of the edge-sharing IrO_6 octahedra and its layered structure. Na atoms are shown in orange, O atoms in red, and Ir atoms in yellow, respectively. The IrO_6 octahedra is shaded in blue. The considered unit cell is represented by the solid black line in both panels. (c) Illustration of the D_{4h} distortion type resulting in a longer O-O apical bond (black) and shorter O-O bonds in the basal plane (gray) (d) Sketch of the Ir atom off-centering resulting in a short Ir-O bond (dark blue) and long Ir-O bonds (light blue) (e) Considered antiferromagnetic spin arrangements for $(2a, 2b, c)$ supercells. Yellow (blue) circles stand for the spin-up (spin-down) magnetic moments, respectively.

each IrO_6 polyhedra's basal plane; one in which the Ir^{4+} ions are “pulled” closer to the Na^+ ions and another in which the Ir^{4+} ions are “pushed” away from the neighboring Ir^{4+} ions in order to reduce the $\text{Ir}^{4+}/\text{Ir}^{4+}$ electrostatic repulsion as shown in Fig. 2(d) with black arrows. Increasing the Ir off-centering increases the Ir-Ir distance along the b axis and reduces the Ir-Ir distances in the a axis direction [see Fig. 2(d)].

To quantify the role of each type of distortion on the magnetism of the Na_2IrO_3 compounds, it is useful to define the D_{4h} distortion and the Ir atom off-centering indices as the ratio

between atomic distances as follows:

$$\delta_{D_{4h}} = \left(\frac{d_{\text{O-O}}^{\text{apical}}}{d_{\text{O-O}}^{\text{basal}}} - 1 \right) \cdot 100, \quad (1)$$

$$\delta_{\text{off}} = \left(\frac{d_{\text{Ir-O}}^{\text{long}}}{d_{\text{Ir-O}}^{\text{short}}} - 1 \right) \cdot 100, \quad (2)$$

where $d_{\text{O-O}}^{\text{apical(basal)}}$ stands for the distance between the O atoms corresponding to the apical(basal) vertices in IrO_6 polyhedra and $d_{\text{Ir-O}}^{\text{long(short)}}$ refer to the length of Ir-O bonds within the basal plane, the long bonds are oriented towards the shared edge between polyhedra and short bonds towards the neighboring Na atom. Both ratios are reported in a percentage ranging from 0%–4%. For the sake of comparison, the reported recent experimental values obtained through x-ray and neutron powder diffraction measurements are $\delta_{D_{4h}} = 1.55\%$ ($\delta_{\text{off}} = 0.67\%$) [26]. Then, to assess the impact of these two types of structural distortions on the magnetic properties of Na_2IrO_3 and quantify it, we construct a model which allow us to increase/reduce the $\delta_{D_{4h}}$ ratio while keeping the average Ir-O bond distance constant; e.g., increasing the length of Ir-O bonds along the D_{4h} distortion's axis in a controlled manner [see arrows in Fig. 2(c)] while reducing the Ir-O bond length in the basal plane in such a way that the average bond length remains constant. Regarding the Ir-atom positions in the IrO_6 's basal plane, an off-centering is present already in the experimental structure. To increase/reduce δ_{off} ratio, the Ir-O bonds corresponding to the edge shared with a NaO_6 polyhedra are reduced/increased [along with the black arrows in Fig. 2(d)]. Nevertheless, at this point we must emphasize that the intent of our model construction is not to reproduce or replicate any experimental results, but simply quantifying the impact of the structural distortions on the magnetic properties of Na_2OIr_3 by tracking the changes on the magnetic ordering and magnetic interactions as a function of these two structural distortion indexes.

B. Magnetic spin structure and exchange interactions

To take into account several magnetic orders beyond ferromagnetism, different supercell sizes are required. As a first step, we dismiss the effects of inter-TMO-layer magnetic interactions as our calculations show they are weak enough to be neglected. Indeed, we built (a,b,2c) supercells and calculated the energy having both ferromagnetic and antiferromagnetic couplings between two neighboring TMO layers, estimating the order of magnitude of the interlayer coupling by their energy difference. These calculations were accomplished based on the experimental structure parameters and within our structural distortion model considering the highest distortion indices ($\delta_{D_{4h}} = 3.98\%$, $\delta_{\text{off}} = 3.92\%$) taking different spin arrangements. We obtain that the interlayer interactions yield an energy difference of less than 1 meV per formula unit, which can be fairly disregarded. The local magnetic interactions are thus analyzed by inspecting the relative stability of different 2D intra-TMO-layers collinear magnetic spin arrangements considered in the (2a,2b,c) supercell [see Fig. 2(e)] as a function of the structural distortions. Upon analyzing the symmetry of the considered structures with

respect to the D_{4h} -elongation axis, we ended up with seven nonequivalent intra-TMO-layers spin orderings. We found that the *zigzag-2* and *zigzag-3* magnetic solutions on the one hand, and the *stripy-2* and *stripy-3* on the other have the same energy. Similarly, for the case of the *armchair*-like structures, i.e., *armchair-2* and *armchair-3* which correspond to a 60° and 120° rotation of the *armchair* configuration, respectively, yielding to similar energy as it is the case for *zigzag-2/zigzag-3* and *stripy-2/stripy-3*. Thus, the *zigzag-3*, *stripy-3*, *armchair-2*, and *armchair-3* configurations are disregarded in the following. (Further information can be seen in Fig. S3 of the Supplemental Material [64].)

III. RESULTS

A. Crystal field versus spin-orbit splitting competition

We first aim to investigate the interplay between the SOC and the CF splitting both existing in Na_2IrO_3 . The CF splitting appears as a consequence of both Jahn-Teller distortions and the TM atoms off-centering due to the presence of Ir^{4+} having a d^5 configuration. At the strong crystal-field regime (i.e., negligible SOC), one can glimpse that the t_{2g} degeneracy is removed through the JT effect, which induces local trigonal distortions in the IrO_6 octahedra. While at a strong SOC regime, the degeneracy is lifted by splitting the $J = 1/2$ from the $J = 3/2$ states. In the latter regime, since the $J = 3/2$ states are filled, the $J = 1/2$ states consist of a linear combination of the t_{2g} states, and no structural distortion is then expected in that case. Therefore, the structural distortion strength emerges as a satisfying gauge to assess whether the material belongs to the strong SOC, crystal-field dominant, or intermediate regime. To investigate the CF-to-SOC regime crossover, we gradually switch on the energy contribution of the SOC interaction using a scalar weight $0 \leq \alpha_{\text{SOC}} \leq 1$ to ponderate it. In this sense, $\alpha_{\text{SOC}} = 0$ would correspond to the nonrelativistic situation where no SOC contribution balances the CF splitting, while for $\alpha_{\text{SOC}} = 1$ the full SOC energy is accounted for. Notice that the variation of the spin and orbital moments as well as the degree of the structural distortions through the δ_{off} and $\delta_{D_{4h}}$ indexes, respectively, are calculated on the relaxed structures. Results are shown in Fig. 3. Starting in the CF-dominant regime with a highly distorted structure for $\alpha_{\text{SOC}} = 0$ ($\delta_{D_{4h}} = 2.6\%$, $\delta_{\text{off}} = 3.8\%$), as the strength of the SOC contribution increases, the structural distortion indexes decrease, as predicted from recent theoretical models [43]. Our results indicate that in the absence of SOC interactions, the JT-induced distortions are needed to abolish the t_{2g} degeneracy. At the opposite limit, when the full SOC contribution is taken into account, both distortions indexes are close to zero ($\delta_{D_{4h}} = 0\%$, $\delta_{\text{off}} = 0.7\%$), implying that the SOC interaction overcomes the JT effect. On the other hand, the TM off-centering distortions, which have an electrostatic origin and thus have less impact on the orbital mixing, are less affected by the SOC interaction, and δ_{off} remains finite even in the strong SOC regime. In fact, recent experimental measurements on resolving the crystal structure for this compound yield to a value for $\delta_{D_{4h}} = 1.6\%$, $\delta_{\text{off}} = 0.7\%$, respectively [26]. Na_2IrO_3 is predicted to be in an intermediate regime when the SOC interaction dominates

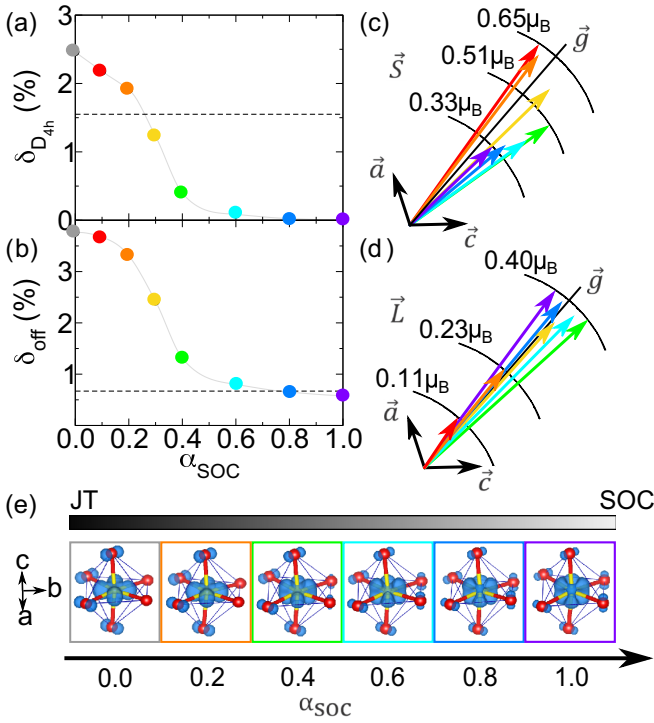


FIG. 3. (a) Jahn-Teller-induced D_{4h} -type structural distortion index ($\delta_{D_{4h}}$), (b) Ir-atom off-centering distortion index (δ_{off}). Dashed lines in (a) and (b) are referred to the experimental values of $\delta_{D_{4h}}$ and δ_{off} for Na_2IrO_3 , respectively. The corresponding direction and magnitude of the spin(orbital) magnetic moments along the ac plane are shown in the insets (c) and (d). The colors of the arrows stand for the SOC strength in agreement with the color code used in the insets (a) and (b). For a sake of comparison, the experimental direction of magnetization \vec{g} , reported in Ref. [40], is also shown. (e) $|m(r)|^2$ isosurface plots as a function of the ponderation weight α_{SOC} of the spin-orbit interaction contribution to the energy. Relativistic self-consistent calculations have been performed allowing both the crystal structure and the direction of magnetization to be optimized at the same time for the zigzag antiferromagnetic magnetic arrangements.

over the CF splitting without nullifying the latter. Hence, both the JT-induced distortions and the Ir off-centering are foreseen to strongly influence the magnetic interactions and the magnetic order even if the SOC remains the dominant interaction. Note that the structure proposed in Ref. [26] has been obtained using both neutron and synchrotron x-ray diffraction patterns and is thus taken as a reference in the present study. The x-ray diffraction pattern, dominated by the Ir-atoms contribution because of its high electron density, complements the neutron powder diffraction measurements used to obtain accurate O and Na atomic positions where the Ir contribution to the diffraction pattern is not ideal as Ir is very absorbent to neutrons. The deviation to the situation where $L = 0$ is quenched and $J = S$, at the CF limit ($\alpha_{\text{SOC}} = 0$), is shown in Figs. 3(c) and 3(d) where the S (L) magnitude decreases (increases), respectively. Moreover, experimental evidence together with theoretical predictions [40,47] show that Na_2IrO_3 exhibits a canted AF magnetization axis along the $g \approx a + c$ direction which corresponds to an angle of $\theta \sim 55^\circ$ with respect to the a axis in the ac plane. Indeed,

our self-consistent relativistic calculations reproduce this result in full agreement. Meaningful orbital contributions to the total magnetic moment were resolved, $\langle \mu_L \rangle \sim 0.4 \mu_B$ while the total magnetic moment was estimated to be $\langle \mu \rangle = 0.74$ Ir/atom, which is inline with the reported by Hou *et al.* [24], who predicted a dominant contribution of the orbital part to the total magnetic moment. Notice that when trying to determine the self-consistent DFT energies for other noncollinear magnetic configurations, we end up with the ground-state magnetic solution. This result can be attributed to the fact that S and L were nonaligned parallel to each other for other quantization axes. The interplay between the JT distortions and the SOC interactions can satisfyingly explain the canted AF ordering stabilization. A similar effect was also predicted for Sr_2IrO_4 [45]. The electronic structure is also expected to be strongly modified along with the CF-to-SOC transition. For $\alpha_{\text{SOC}} = 0$, the orbital carrying the magnetic moment (i.e., the minority spin LUMO) corresponds to pure d_{xy} orbitals when considering a JT elongation axis along the z direction. As shown in Fig. 3(e), by increasing the α_{SOC} strength, the weight of the d_{xy} orbitals in the minority spin LUMO decreases to ultimately achieve a similar weight as the d_{xz} and d_{yz} orbitals, reaching an almost isotropic magnetization density profile which is consistent with the onset of the $J_{\text{eff}} = 1/2$ state in the Ir^{4+} atoms. The change of the shape of the magnetization density from a highly anisotropic in the CF regime to a quasi-isotropic is expected to affect the magnetic interactions strongly. Notably, the anisotropic character of the magnetic density induces directional and bond-dependency anisotropy in the magnetic interactions together with variations in their magnitude, as it will be shown in the next section.

B. Influence of the structural distortions on the magnetic interactions

To further investigate the effects of structural distortions on the magnetic interactions and magnetic order, we deliberately turn off the SOC interactions from our calculations. Thus, nonrelativistic collinear calculations were done to determine the ground-state structure and the lowest-lying magnetic textures by optimizing the Na_2IrO_3 crystal structure taking simultaneously different U_{eff} values and ferromagnetic (FM) and antiferromagnetic (AF) spin arrangements [see Fig. 2(e)]. In Table I we present the considered magnetic structures as a function of the two different local distortions $\delta_{D_{4h}}$ and δ_{off} , for different U_{eff} values. We disclose a steady $\delta_{D_{4h}}$ index $\sim 2\% - 3\%$ for all structures in the insulating regime, which is larger than the index of the experimental structure ($\delta_{D_{4h}} = 1.55\%$). Furthermore, we find that when U_{eff} is weak, the variations of $\delta_{D_{4h}}$ are modest (between 0% and 2%) depending the considered magnetic order. Besides, we observe that the experimental D_{4h} distortion axis holds for most cases (the polyhedra's D_{4h} elongation axis aligning parallel in the supercell along the local z axis). Exceptions were found for the ferromagnetic configuration ($U_{\text{eff}} = 1$ eV) where $\delta_{D_{4h}} = 0.09\%$, in the zigzag-2 antiferromagnetic spin arrangement where the polyhedra were weakly distorted, and the armchair antiferromagnetic for which the polyhedra have their local elongations along the x, y axes. Concerning the Ir-atom off-centering δ_{off} , we found

TABLE I. Magnetic collinear-structures distortion indices obtained upon optimization of the Na_2IrO_3 supercells for $U_{\text{eff}} = 1, 2, 3,$ and 4 eV. All index values are given in percentage. Structures marked with * were found in the metallic regime. For sake of comparison, the experimental structure has $\delta_{D_{4h}} = 1.55\%$ and $\delta_{\text{off}} = 0.67\%$.

	$U_{\text{eff}} = 1$ eV	$U_{\text{eff}} = 2$ eV	$U_{\text{eff}} = 3$ eV	$U_{\text{eff}} = 4$ eV
		$\delta_{D_{4h}}$ (%)		
fm	0.09*	2.09	2.69	2.89
zigzag	1.36*	2.46	2.72	2.92
zigzag-2	0.25*	2.30	2.74	2.93
armchair	0.77	2.28	2.75	2.93
stripy	0.72*	2.24	2.81	2.97
stripy-2	1.05*	2.36	2.78	2.96
Néel	1.43*	2.48	2.83	2.99
		δ_{off} (%)		
fm	0.54*	3.34	3.78	3.73
zigzag	2.85*	3.76	3.85	3.80
zigzag-2	0.70*	3.77	3.80	3.74
armchair	0.35	3.73	3.82	3.75
stripy	1.91*	3.75	3.80	3.74
stripy-2	2.41*	3.83	3.89	3.83
Néel	2.87*	3.81	3.85	3.80

values between $\sim 3.3\%$ – 3.8% in the insulating regime that are much larger than those of the experimental structure ($\delta_{\text{off}} \sim 0.67\%$). All together, it shows that the structural distortion strength, electronic regime (metallic or insulating), and the magnetic order is intimately related through microscopical mechanisms, which deserve to be further investigated. The overestimation of the structural distortion indexes compared to the available experimental data is entirely inline with the results presented above concerning the interplay between the CF splitting and the SOC interactions. In the following we quantify the influence of the structural distortions on the magnetic interactions and the ground state's magnetic order through the structural-distortion-dependent model. We calculated the energy of the nonrelaxed structures having different $\delta_{D_{4h}}$ and δ_{off} indexes and several magnetic orderings as shown in Fig. 2(e) (fixed-structure self-consistent calculations) to identify the low-lying magnetic spin arrangements close to the ground state (GS) resulting in a sort of magnetic phase diagrams in the $\delta_{D_{4h}} - \delta_{\text{off}}$ space. The magnetic phase diagrams as a function of the $\delta_{D_{4h}}, \delta_{\text{off}}$ indexes are presented in Fig. 4. Dimerization of Na_2IrO_3 due to long-range interactions as predicted by some quantum J_1 - J_2 - J_3 models [72] is unlikely and should be discarded for any degree of distortion. The presence of nonisotropic interactions in Na_2IrO_3 does not seem to promote the occurrence of dimers. Besides, to our knowledge, there is no experimental evidence to support dimerization for this compound. We found that the competition between the ferromagnetic and zigzag antiferromagnetic configurations emerges depending on the local polyhedra's distortion, other magnetic solutions are significantly higher in energy (see Fig. S4 of the Supplemental Material [64]). Our results demonstrate that the magnetic ordering of the ground-state structure is extremely sensitive to the local-distortion indices. Notice that the obtained phase diagrams are nontrivial and provide a clear evidence that the local distortions drive

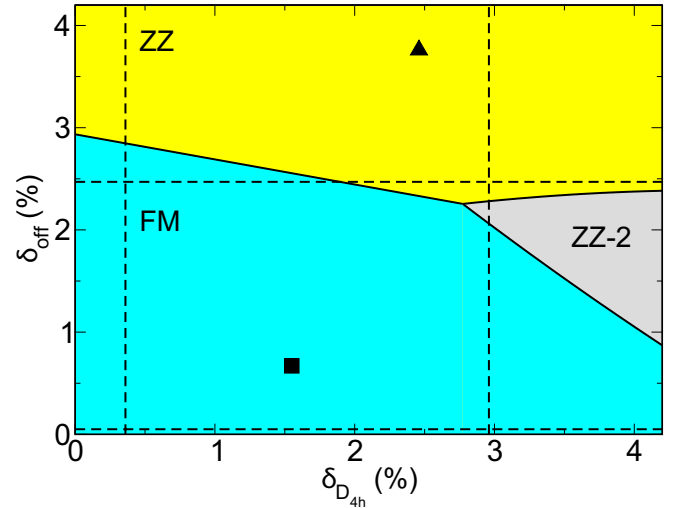


FIG. 4. Magnetic-phase $\delta_{D_{4h}}$ - δ_{off} diagram where the relative magnetic ground state (GS) is shown depending on the $\delta_{D_{4h}}$ and δ_{off} values at $U_{\text{eff}} = 2$ eV. As a reference, the experimental structure's distortion indices are marked by a square. Optimized structure's distortion values for the zigzag (ZZ) magnetic ground state is marked by a triangle.

the magnetism of Na_2IrO_3 . Furthermore, the magnitude and variations of the magnetic energy due to the exchange couplings are calculated. For the considered seven nonequivalent magnetic solutions, one can split the different contributions in bond-dependent magnetic interaction energies (MIE) up to the third NNs. As the JT-elongation axis aligns in the ac plane, the MIE along the b axis and along the ab plane is found to be different for the NN. To corroborate this statement, we show in Fig. 5(a) the highly anisotropic magnetization density for the relaxed zigzag magnetic solution. The bond-directional NN magnetic interaction energy ΔE_1^b (ΔE_1^{ab}) along the b direction (ab plane) can be assessed using the following relation: $\Delta E_1^b = (E_{\text{fm}} - E_{\text{zz}} + 2E_{\text{zz-2}} - E_{\text{Néel}} + E_{\text{str}} - 2E_{\text{str-2}})/4$ ($\Delta E_1^{ab} = (E_{\text{fm}} + E_{\text{zz}} - E_{\text{Néel}} - E_{\text{str}})/4$), respectively, where E_X corresponds to the calculated energy of Na_2IrO_3 at fixed structure and having a given magnetic configuration ($X = \text{fm}, \text{zz}, \text{zz-2}, \text{Néel}, \text{str}, \text{str-2},$ and arm). We present in Fig. 5 both NN bond-directional MIE together with the integrated projected COOP (IpCOOP) along pertinent Ir-O bonds [highlighted in Fig. 5(a)] as a function of the distortion parameters. At the weakly distorted limit, ΔE_1^b and ΔE_1^{ab} should have an equivalent magnitude for symmetry reasons that would also be the case in the strong SOC regime where structural distortions are suppressed. When increasing the Ir-atom off-centering distortion, ΔE_1^{ab} remains quasiconstant while ΔE_1^b decreases significantly. As a function of the D_{4h} distortion, both ΔE_1^b slightly decrease while ΔE_1^{ab} decrease significantly. To unveil a microscopic origin to the observed behavior, we calculated the COOP (IpCOOP) over the first unoccupied band. Thus, we measure the overlap between the orbitals which carry the magnetic moment and obtain information regarding the strength and behavior of direct or indirect exchange mechanisms with respect to the distortion indexes. The Ir-O IpCOOP between iridium and oxygen along the b direction remains constant when

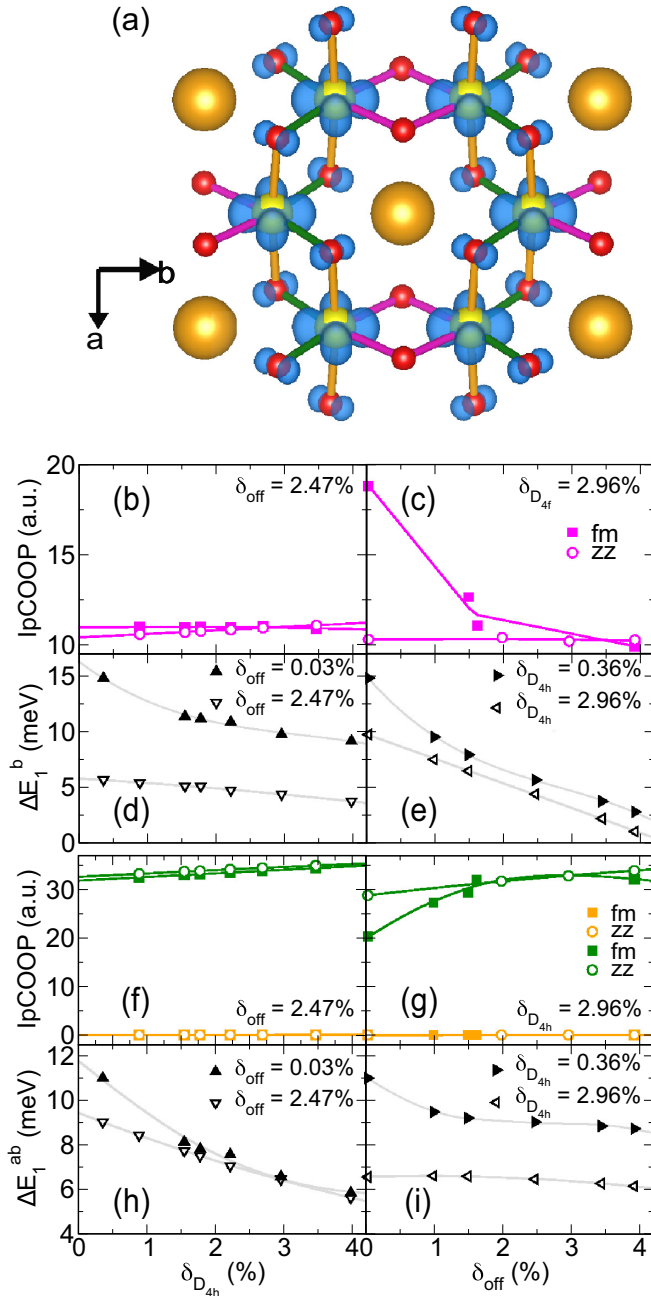


FIG. 5. (a) Magnetization density for the relaxed *zigzag* magnetic ground-state arrangement of Na₂IrO₃. (b) and (c) and (f) and (g) Integrated projected crystal orbital overlap population (IpCOOP) for the ferromagnetic and *zigzag* spin configurations having some representative structure's distortion indices. (d) and (e) Bond-directional NN magnetic interaction energy ΔE_1^b along the *b* direction. (h) and (i) Bond-directional NN magnetic interaction energy ΔE_1^{ab} along the *ab* plane at $\delta_{\text{off}} = 0.03\%$ (2.47%) and $\delta_{D_{4h}} = 0.36\%$ (2.96%), respectively.

increasing the D_{4h} distortion index but significantly decreases when the off-centering index increases. The decrease of ΔE_1^b when increasing the Ir-atom off-centering index is then mainly due to a lower contribution of the Hund coupling. Indeed, the Ir-atom off-centering increases the Ir-Ir distances along the *b* axis. On the contrary, the oxygen-mediated superex-

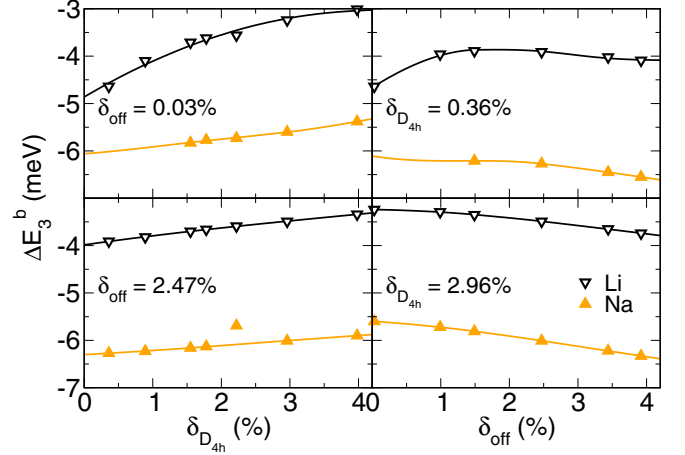


FIG. 6. Bond-directional third-NN magnetic interaction energies ΔE_3^b along the *b* direction at $\delta_{\text{off}} = 0.03\%$ (2.47%) and $\delta_{D_{4h}} = 0.36\%$ (2.96%), respectively, having Li and Na atoms as alkali elements in the Ir-layered-honeycomb hexagonal lattice.

change mechanism appears to be far weaker than the Hund coupling since the decrease of the Ir-O overlap would decrease an AF-like contribution and thus increase ΔE_1^b . Concerning ΔE_1^{ab} , it shows that there is also no oxygen-mediated superexchange along the Ir-Ir path so that ΔE_1^{ab} only arise from the Hund ferromagnetic coupling but is weakly affected by the off-centering distortion. Besides, the cancellation of the oxygen-mediated superexchange along the Ir-Ir path discards the occurrence of sizable second NN interactions as seen in Fig. 5 and Fig. S6 of the Supplemental Material [64], respectively. The direct Ir-Ir AF-like exchange mechanism is also discarded since the obtained IpCOOPs between neighboring Ir atoms are even weaker than the IpCOOPs between Ir-O (see Figs. S7 and S8 of the Supplemental Material [64]). The third NN (3NN) MIE are also bond and directional dependent, yet due to the JT-induced polarization of the magnetic density. We define the 3NN magnetic interaction energy along the *b* axis as $\Delta E_3^b = (E_{\text{arm}} - E_{\text{ZZ}-2})$ and along the *ab* plane as $\Delta E_3^{ab} = (E_{\text{fm}} - E_{\text{ZZ}} + 2E_{\text{ZZ}-2} - E_{\text{Néel}} + E_{\text{str}} + 2E_{\text{str}-2} - 4E_{\text{arm}})/8$. Remarkably, we find that the *b*-bond directional 3NN MIE (ΔE_3^b) are of the same order of magnitude as the first NN magnetic interaction energy (ΔE_1^b), favoring the antiferromagnetism. We disclose its microscopic nature by substituting the Na atoms in the compound for another light alkali metal (Li). Li atoms are smaller and more electronegative. The Na-to-Li substitution drastically decreases the value of ΔE_3^b indicating that the alkali metal mediates the ΔE_3^b magnetic interaction energy through a superexchange mechanism as shown in Fig. 6. The value of ΔE_3^b slightly decreases when $\delta_{D_{4h}}$ increases, probably due to the electron localization induced by an enhanced JT effect. On the contrary, ΔE_3^b increases when δ_{off} increases since the Ir-Na distance decreases along the *b* direction. Importantly, ΔE_3^{ab} is far weaker than ΔE_3^b due to the orbital polarization induced by the JT effect. The difference between ΔE_3^{ab} and ΔE_3^b should be reduced when the SOC strength increases as the magnetization density becomes more isotropic as can be seen in Fig. 3. Summarizing, the magnetic ordering can be understood through the

magnetic interaction energies ΔE_1^b , ΔE_1^{ab} , and ΔE_3^b . Only the competition between FM, ZZ, and ZZ-2 magnetic orders is relevant, considering FM NN, and AF 3NN interactions (see Fig. S5 of the Supplemental Material [64]).

IV. DISCUSSION AND CONCLUSIONS

We have carried out a thorough investigation regarding the magnetism of Na_2IrO_3 . We analyze in particular the underlying interplay between the SOC and the CF splitting. Our calculations, together with experimental measurements, suggest that the spin-orbit interactions do not fully overcome the CF splitting in these compounds. We have conducted in Sec. III B noncollinear calculations to reckon the effects of the CF-induced structural distortions on the local magnetic interactions. In light of these findings, we conclude that: (i) the structural distortions induce highly anisotropic bond and directional-dependent magnetic interactions, (ii) NN FM interactions are dominated by the Hund coupling and are influenced by the structural distortions as they have a substantial impact on the Ir-Ir bonding distances, and (iii) 3NN AF-like interactions are mediated by the alkali atoms being affected to a lesser extent by structural distortions. Altogether we disclose that the *zigzag* magnetic order can be stabilized due to the structural distortion-induced bond dependency of the magnetic interactions. To provide a global portrait concerning the magnetism of Na_2IrO_3 , we start from the most simple picture, i.e., without considering any structural distortions (perfect local IrO_6 -octahedra) and no SOC. Following the Goodenough-Kanamori rules, Na_2IrO_3 is expected to be a ferromagnetic compound as the 90° Ir-O-Ir angle preclude efficient first NN antiferromagnetic superexchange interactions. Indeed, our noncollinear calculations demonstrate that at low-structural distortion level, the three t_{2g} orbitals are degenerate (metallic regime) so that the magnetic moment is carried by a quasi-isotropic linear combination of the three t_{2g} orbitals, as shown in Fig. 7. As the D_{4h} distortion becomes substantial, the magnetic moment is carried by the anisotropic t_{2g} orbitals perpendicular to the JT axis, see Fig. 7. We have revealed that this distortion first discriminates the bond/direction-dependent magnetic interactions but also endeavors the first NN and the 3NN magnetic interactions. From an orbital point of view, the Ir off-centering is foreseen to have a weak effect over the t_{2g} -orbitals splitting, but it has been established to balance the strength between the first NN Hund ferromagnetic exchange interaction and 3NN alkali-mediated AF interaction. Despite triggering the SOC interaction and even at the strong SOC regime ($\alpha_{\text{SOC}} = 1$), the above analysis still remains. Indeed, as presented in Fig. 7, the magnetization density profile is affected by the local structural distortions. At low-distortion indices, we observe that the magnetization is carried by a linear combination of the three t_{2g} orbitals, following a similar behavior as it is expected for a pure $J_{\text{eff}} = 1/2$ system. At this limit, owing to the isotropic character of the magnetization density, only a weak bond/directional dependency on the magnetic interactions is anticipated. Consequently, the energy difference between the *zigzag* and *zigzag-2* magnetic solutions is expected to be barely perceptible, yielding to paramagnetism at very low temperatures. Indeed, in that case, our calcula-

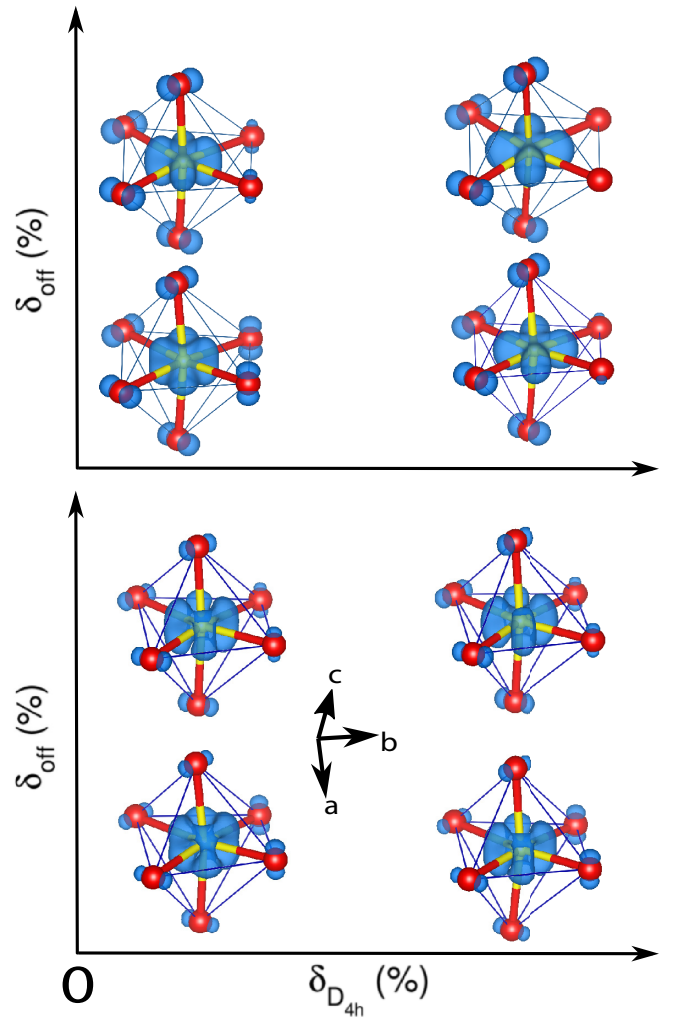


FIG. 7. Orbital-selectivity magnetization density diagram as a function of the local distortions $\delta_{D_{4h}}$ and δ_{off} strength, for the non-relativistic (upper panel) and relativistic (under panel) regimes.

tions show that the energy difference between the *zigzag* and *zigzag-2* magnetic spin configurations is less than 1 meV. When the distortion indices increase the weight of the d_{xy} orbitals increases, thus deviating from the perfect $J_{\text{eff}} = 1/2$ state and the bond/direction dependency of magnetic interactions should increase. The previous scenario, having dominant SOC interactions but reminiscent structural distortions, is supported by recent experimental structural characterizations [26], particularly by the work of Chun and co-workers who state that the critical temperature in Na_2IrO_3 is limited by the anisotropic interactions rather than the interlayer coupling and the *zigzag* correlations survive on a length scale of several nanometers (approximately three unit cells wide) above the Néel temperature [40]. In summary, based on our calculations, the formation of the *zigzag* phase can solely be attributed to the inherent structural distortions. Moreover, it also suggests that in the quest for quantum spin-liquid phases, the materials which exhibit a bias to display JT-type distortions should be discarded from the potential candidates unless the SOC interactions fully overcome the resulting structural distortions.

Herein, we have used the flexibility provided by the DFT addressing the structural relaxations and investigated

the inherent structural-dependent phenomena regarding the magnetic properties of Na_2IrO_3 . The Heisenberg-Kitaev Hamiltonian seems to be suitable for scrutinizing both thermodynamic and response functions such as the Weiss constant and or the magnetic susceptibility compared with experimental measurements [54]. Nevertheless, such Hamiltonian (and other more sophisticated models) is typically parametrized with a particular fixed crystal structure. Our results suggest that the exchange interactions are susceptible to the local structural distortions independently of the SOC interaction strength, particularly the NN Hund coupling and the 3NN AF-exchange interactions. Indeed, such changes in the magnetic interactions as a function of the local distortions should drastically affect the parameters of the HK model. Therefore, a careful lookout at the crystal structure should be done prior to the parametrization. A structure-dependent parametrization of a HK model can be envisioned but remains beyond the scope of this work. As a final remark, our results

also appeal on resolving highly accurate experimental crystal structures, particularly those obtained combining both neutron and synchrotron x-ray diffraction patterns as they constitute the baseline for understanding the microscopic physical properties of this type of compound.

ACKNOWLEDGMENTS

The authors thankfully acknowledge the computer resources, technical expertise, and support provided by the by Laboratorio Nacional de Supercómputo del Sureste de México (LNS) Project No. 201703117n. The authors acknowledge support from a bilateral cooperation SEP-CONACYT Mexico-ANUIES-ECOS NORD France (Grant No. 296636/M18P02). The authors also thank Dr. Romain Berthelot for fruitful discussions and J. Rentería-Arriaga and J. C. Sánchez-Leaños for their technical support.

-
- [1] L. Janssen, E. C. Andrade, and M. Vojta, *Phys. Rev. Lett.* **117**, 277202 (2016).
- [2] S. C. Williams, R. D. Johnson, F. Freund, S. Choi, A. Jesche, I. Kimchi, S. Manni, A. Bombardi, P. Manuel, P. Gegenwart, and R. Coldea, *Phys. Rev. B* **93**, 195158 (2016).
- [3] Y. Li, S. M. Winter, H. O. Jeschke, and R. Valentí, *Phys. Rev. B* **95**, 045129 (2017).
- [4] S. Ducatman, I. Rousochatzakis, and N. B. Perkins, *Phys. Rev. B* **97**, 125125 (2018).
- [5] S. Choi, S. Manni, J. Singleton, C. V. Topping, T. Lancaster, S. J. Blundell, D. T. Adroja, V. Zapf, P. Gegenwart, and R. Coldea, *Phys. Rev. B* **99**, 054426 (2019).
- [6] K. Hu, Z. Zhou, Y.-W. Wei, C.-K. Li, and J. Feng, *Phys. Rev. B* **98**, 100103(R) (2018).
- [7] M. Majumder, R. S. Manna, G. Simutis, J. C. Orain, T. Dey, F. Freund, A. Jesche, R. Khasanov, P. K. Biswas, E. Bykova, N. Dubrovinskaia, L. S. Dubrovinsky, R. Yadav, L. Hozoi, S. Nishimoto, A. A. Tsirlin, and P. Gegenwart, *Phys. Rev. Lett.* **120**, 237202 (2018).
- [8] V. Hermann, J. Ebad-Allah, F. Freund, I. M. Pietsch, A. Jesche, A. A. Tsirlin, J. Deisenhofer, M. Hanfland, P. Gegenwart, and C. A. Kuntscher, *Phys. Rev. B* **96**, 195137 (2017).
- [9] G. Simutis, N. Barbero, K. Rolfs, P. Leroy-Calatayud, K. Mehawat, R. Khasanov, H. Luetkens, E. Pomjakushina, Y. Singh, H. R. Ott, J. Mesot, A. Amato, and T. Shiroka, *Phys. Rev. B* **98**, 104421 (2018).
- [10] R. Yadav, S. Rachel, L. Hozoi, J. van den Brink, and G. Jackeli, *Phys. Rev. B* **98**, 121107(R) (2018).
- [11] H. Liu and G. Khaliullin, *Phys. Rev. Lett.* **122**, 057203 (2019).
- [12] S. D. Das, S. Kundu, Z. Zhu, E. Mun, R. D. McDonald, G. Li, L. Balicas, A. McCollam, G. Cao, J. G. Rau, H.-Y. Kee, V. Tripathi, and S. E. Sebastian, *Phys. Rev. B* **99**, 081101(R) (2019).
- [13] K. Slagle, W. Choi, L. E. Chern, and Y. B. Kim, *Phys. Rev. B* **97**, 115159 (2018).
- [14] M. Hermanns, I. Kimchi, and J. Knolle, *Annu. Rev. Condens. Matter Phys.* **9**, 17 (2018).
- [15] T. Birol, K. Haule, and D. Vanderbilt, *Phys. Rev. B* **98**, 134432 (2018).
- [16] R. Yadav, M. S. Eldeeb, R. Ray, S. Aswartham, M. I. Sturza, S. Nishimoto, J. van den Brink, and L. Hozoi, *Chem. Sci.* **10**, 1866 (2019).
- [17] R. Sano, Y. Kato, and Y. Motome, *Phys. Rev. B* **97**, 014408 (2018).
- [18] C. Vallée, M. Saubanére, P. Sanz-Camacho, Y. Biecher, B. Fraisse, E. Suard, G. Rousse, D. Carlier, and R. Berthelot, *Inorg. Chem.* **58**, 11546 (2019).
- [19] S. Okamoto and D. Xiao, *J. Phys. Soc. Jpn.* **87**, 041006 (2018).
- [20] K. Foyevtsova, H. O. Jeschke, I. I. Mazin, D. I. Khomskii, and R. Valentí, *Phys. Rev. B* **88**, 035107 (2013).
- [21] L. Xu, R. Yadav, V. Yushankhai, L. Siurakshina, J. van den Brink, and L. Hozoi, *Phys. Rev. B* **99**, 115119 (2019).
- [22] M. Abramchuk, C. Ozsoy-Keskinbora, J. W. Krizan, K. R. Metz, D. C. Bell, and F. Tafti, *J. Am. Chem. Soc.* **139**, 15371 (2017).
- [23] V. Hermann, M. Altmeyer, J. Ebad-Allah, F. Freund, A. Jesche, A. A. Tsirlin, M. Hanfland, P. Gegenwart, I. I. Mazin, D. I. Khomskii, R. Valentí, and C. A. Kuntscher, *Phys. Rev. B* **97**, 020104(R) (2018).
- [24] Y. S. Hou, J. H. Yang, H. J. Xiang, and X. G. Gong, *Phys. Rev. B* **98**, 094401 (2018).
- [25] L. Hao, D. Meyers, M. P. M. Dean, and J. Liu, *J. Phys. Chem. Solids* **128**, 39 (2017).
- [26] A. J. Perez, D. Batuk, M. Saubanére, G. Rousse, D. Foix, E. McCalla, E. J. Berg, R. Dugas, K. H. V. D. Bos, M. L. Doublet, D. Gonbeau, A. M. Abakumov, G. V. Tendeloo, and J. M. Tarascon, *Chem. Mater.* **28**, 8278 (2016).
- [27] I. Rousochatzakis and N. B. Perkins, *Phys. Rev. B* **97**, 174423 (2018).
- [28] J. Rusnačko, D. Gotfryd, and J. Chaloupka, *Phys. Rev. B* **99**, 064425 (2019).
- [29] A. Revelli, M. Moretti Sala, G. Monaco, C. Hickey, P. Becker, F. Freund, A. Jesche, P. Gegenwart, T. Eschmann, F. L. Buessen, S. Trebst, P. H. M. van Loosdrecht, J. van

- den Brink, and M. Grüninger, *Phys. Rev. Res.* **2**, 043094 (2020).
- [30] Y. Singh and P. Gegenwart, *Phys. Rev. B* **82**, 064412 (2010).
- [31] G. Jackeli and G. Khaliullin, *Phys. Rev. Lett.* **102**, 017205 (2009).
- [32] J. Chaloupka, G. Jackeli, and G. Khaliullin, *Phys. Rev. Lett.* **105**, 027204 (2010).
- [33] H. A. Jahn and E. Teller, *Proc. R. Soc. London Ser. A* **161**, 220 (1937).
- [34] A. Shitade, H. Katsura, J. Kuneš, X.-L. Qi, S.-C. Zhang, and N. Nagaosa, *Phys. Rev. Lett.* **102**, 256403 (2009).
- [35] S. K. Choi, R. Coldea, A. N. Kolmogorov, T. Lancaster, I. I. Mazin, S. J. Blundell, P. G. Radaelli, Y. Singh, P. Gegenwart, K. R. Choi, S. W. Cheong, P. J. Baker, C. Stock, and J. Taylor, *Phys. Rev. Lett.* **108**, 127204 (2012).
- [36] F. Ye, S. Chi, H. Cao, B. C. Chakoumakos, J. A. Fernandez-Baca, R. Custelcean, T. F. Qi, O. B. Korneta, and G. Cao, *Phys. Rev. B* **85**, 180403(R) (2012).
- [37] G. L. Stamokostas and G. A. Fiete, *Phys. Rev. B* **97**, 085150 (2018).
- [38] R. Comin, G. Levy, B. Ludbrook, Z.-H. Zhu, C. N. Veenstra, J. A. Rosen, Y. Singh, P. Gegenwart, D. Stricker, J. N. Hancock, D. van der Marel, I. S. Elfimov, and A. Damascelli, *Phys. Rev. Lett.* **109**, 266406 (2012).
- [39] H.-J. Kim, J.-H. Lee, and J.-H. Cho, *Sci. Rep.* **4**, 5253 (2014).
- [40] S. Hwan Chun, J.-W. Kim, J. Kim, H. Zheng, C. C. Stoumpos, C. D. Malliakas, C. D., J. F. Mitchell, K. Mehlawat, Y. Singh, Y. Choi, T. Gog, A. Al-Zein, M. M. Sala, M. Krisch, J. Chaloupka, G. Jackeli, G. Khaliullin, and B. J. Kim, *Nat. Phys.* **11**, 462 (2015).
- [41] S. Bhattacharjee, S.-S. Lee, and Y. B. Kim, *New J. Phys.* **14**, 073015 (2012).
- [42] C. H. Sohn, H.-S. Kim, T. F. Qi, D. W. Jeong, H. J. Park, H. K. Yoo, H. H. Kim, J.-Y. Kim, T. D. Kang, D.-Y. Cho, G. Cao, J. Yu, S. J. Moon, and T. W. Noh, *Phys. Rev. B* **88**, 085125 (2013).
- [43] S. V. Streltsov and D. I. Khomskii, *Phys. Rev. X* **10**, 031043 (2020).
- [44] E. E. Gordon, H. Xiang, J. Köhler, and M.-H. Whangbo, *J. Chem. Phys.* **144**, 114706 (2016).
- [45] P. Liu, S. Khmelevskiy, B. Kim, M. Marsman, D. Li, X.-Q. Chen, D.D. Sarma, G. Kresse, and C. Franchini, *Phys. Rev. B* **92**, 054428 (2015).
- [46] X. Xi, X. Bo, X. S. Xu, P. P. Kong, Z. Liu, X. G. Hong, C. Q. Jin, G. Cao, X. Wan, and G. L. Carr, *Phys. Rev. B* **98**, 125117 (2018).
- [47] K. Hu, F. Wang, and J. Feng, *Phys. Rev. Lett.* **115**, 167204 (2015).
- [48] D. Fiore Mosca, L. V. Pourovskii, B. H. Kim, P. Liu, S. Sanna, F. Boscherini, S. Khmelevskiy, and C. Franchini, *Phys. Rev. B* **103**, 104401 (2021).
- [49] M. Laubach, J. Reuther, R. Thomale and S. Rachel, *Phys. Rev. B* **96**, 121110(R) (2017).
- [50] T. Okubo, K. Shinjo, Y. Yamaji, N. Kawashima, S. Sota, T. Tohyama, and M. Imada, *Phys. Rev. B* **96**, 054434 (2017).
- [51] Y. Yamaji, Y. Nomura, M. Kurita, R. Arita, and M. Imada, *Phys. Rev. Lett.* **113**, 107201 (2014).
- [52] Y. Li, K. Foyevtsova, H. O. Jeschke, and R. Valentí, *Phys. Rev. B* **91**, 161101(R) (2015).
- [53] I. I. Mazin, H. O. Jeschke, K. Foyevtsova, R. Valentí, and D. I. Khomskii, *Phys. Rev. Lett.* **109**, 197201 (2012).
- [54] S. M. Winter, Y. Li, H. O. Jeschke, and R. Valentí, *Phys. Rev. B* **93**, 214431 (2016).
- [55] G. Kresse and J. Hafner, *Phys. Rev. B* **47**, 558(R) (1993).
- [56] G. Kresse and J. Hafner, *Phys. Rev. B* **49**, 14251 (1994).
- [57] G. Kresse and J. Furthmüller, *Comput. Mater. Sci.* **6**, 15 (1996).
- [58] G. Kresse and J. Furthmüller, *Phys. Rev. B* **54**, 11169 (1996).
- [59] J. P. Perdew, K. Burke, and M. Ernzerhof, *Phys. Rev. Lett.* **77**, 3865 (1996).
- [60] J. P. Perdew, K. Burke, and M. Ernzerhof, *Phys. Rev. Lett.* **78**, 1396(E) (1997).
- [61] P. E. Blöchl, *Phys. Rev. B* **50**, 17953 (1994).
- [62] G. Kresse and D. Joubert, *Phys. Rev. B* **59**, 1758 (1999).
- [63] S. L. Dudarev, G. A. Botton, S. Y. Savrasov, C. J. Humphreys, and A. P. Sutton, *Phys. Rev. B* **57**, 1505 (1998).
- [64] See Supplemental Material at <http://link.aps.org/supplemental/10.1103/PhysRevB.105.094413> for the calculated lattice parameters, further band gap plots, electrostatic energy curve, energy equivalence of zigzag and stripy spin arrangements, relative stability of ground states, metal-to-insulator and magnetic phase diagrams, integrated COOPs, and effective spin parameters.
- [65] S. Grimme, J. Antony, S. Ehrlich, and H. Krieg, *J. Chem. Phys.* **132**, 154104 (2010).
- [66] S. Grimme, S. Ehrlich, and L. Goerigk, *J. Comput. Chem.* **32**, 1456 (2011).
- [67] R. Dronskowski and P. E. Blöchl, *J. Phys. Chem.* **97**, 8617 (1993).
- [68] V. L. Deringer, A. L. Tchougréeff, and R. Dronskowski, *J. Phys. Chem. A* **115**, 5461 (2011).
- [69] S. Maintz, V. L. Deringer, A. L. Tchougréeff, and R. Dronskowski, *J. Comput. Chem.* **34**, 2557 (2013).
- [70] S. Maintz, M. Esser, and R. Dronskowski, *Acta Phys. Pol. B* **47**, 1165 (2016).
- [71] R. Nelson, C. Ertural, J. George, V. L. Deringer, G. Hautier, and R. Dronskowski, *J. Comput. Chem.* **41**, 1931 (2020).
- [72] J. B. Fouet, P. Sindzingre, and C. Lhuillier, *Eur. Phys. J. B* **20**, 241 (2001).